A 91-Channel Hyperspectral LiDAR for Coal/Rock Classification

Hui Shao, Yuwei Chen, Zhirong Yang, Changhui Jiang, Wei Li, Haohao Wu, Zhijie Wen, Shaowei Wang, Eetu Puttnon, and Juha Hyyppä

***Abstract*— During the mining operation, it is a critical task in coal mines to significantly improve the safety by precision coal mining sorting and rock classification from different layers. It implies that a technique for rapidly and accurately classifying coal/rock in-site needs to be investigated and established, which is of significance for improving the coal mining efficiency and safety. In this letter, a 91-channel hyperspectral LiDAR (HSL) using an acousto-optic tunable filter (AOTF) as the spectroscopic device is designed, which operates based on the wide-spectrum emission laser source with a 5-nm spectral resolution to tackle this issue. The spectra of four-type coal/rock specimens collected by HSL are used to classify with three multi-label classifiers: naive Bayes (NB), logistic regression (LR), and support vector machine (SVM). Furthermore, we discuss and explore whether Gaussian fitting (GF) method and calibration with the reference whiteboard (RB) can enhance the classification accuracy. The experimental results show that the GF technique not only improves the accuracy of range measurement but also optimizes the classification performance using the spectra collected by the HSL. In addition, calibration with RB can improve classification accuracy as well. In addition, we also discuss methods to improve the calibration-free classification accuracy preliminarily.**

***Index Terms*— Acousto-optic tunable filter (AOTF), coal/rock classification, Gaussian fitting (GF), hyperspectral LiDAR (HSL).**

I. Introduction

SOFT rock mining belongs to the group of mining techniques used to extract coal, oil shale, potash, and other minerals from underground sedimentary rocks. As one of the most important soft rock ores, coal counts approximately 70% of the primary energy consumption in China today [1]. However, the casualty of the coal mining accidents is also enormous. It is anticipated to adopt modern practices to significantly improve the safety in coal mines. Especially, the application of laser scanning technology is used to verify spatial changes of underground mining works, to assess stability conditions of mining workplaces [2], to detect large-scale deformation [3], and to monitor the strata surface displacements during and after mining [4]. A laser scanner is also a powerful tool for classification, identifying, and recording the condition of coal rocks, which is beneficial to mine safety [5], [6].

Most laser scanners operate at a single wavelength providing accurate point clouds data with a high spatial resolution and the intensity data of the employed wavelength, which is widely used in 3-D reconstruction and allowed object classification based on their geometric properties [7] or spectral characterization [8], whereas the monochromatic system configuration of the traditional LiDAR strongly restricts the performance of application.

Active hyperspectral LiDAR (HSL) [9]–[11] can collect the object point cloud information with abundant spectral profile, which is more beneficial to target classification than the traditional LiDAR sensors operating with a single-wavelength laser source. However, the applicability of previously developed HSLs is strongly restricted due to their limited and discrete spectral channels. To solve this problem, an acousto-optic tunable filter (AOTF)-based HSL, termed as AOTF-HSL, is designed, with a 5-nm spectral resolution, resulting in a 91-channel HSL covering from 650 to 1100 nm. We investigated its capability for coal/rock classification based on three

Manuscript received May 28, 2019; revised July 22, 2019; accepted July 23, 2019. This work was supported in part by the Academy of Finland Projects "Centre of Excellence in Laser Scanning Research (CoE-LaSR)" under Project 307362, in part by the "New Laser and Spectral Field Methods for In Situ Mining and Raw Material Investigations" under Project 292648, Project 314177, and Project 307929, in part by the Ministry of Science and Technology under Grant 2017YFC1405401, in part by the Chinese Academy of Science under Grant 181811KYSB20160113, in part by the Chinese Ministry of Science and Technology under Grant 2015DFA70930, in part by the Shanghai Science and Technology Foundations under Grant 18590712600, in part by the Anhui Natural Science Foundation under Grant KJ2019A0767 and Grant 1804d08020314, in part by the Doctoral Program of Anhui Jianzhu University under Grant 2015QD07 and Grant JZ192007, in part by the Anhui and Jiangsu Province Key Laboratory Research Found under Grant 2017kfkt009 and Grant 2019-157, in part by the Shandong Natural Science Foundation under Grant ZR2019YQ26, in part by the Qingdao Natural Science Foundation under Grant 18-2-2-68-jch, and in part by the Research Council of Norway under Project 287284. *(Corresponding authors: Yuwei Chen; Zhijie Wen.)*

H. Shao is with the School of Electronic and Information Engineering, Anhui Jianzhu University, Hefei 230601, China, and also with the Department of Remote Sensing and Photogrammetry, Finnish Geospatial Research Institute, FI-02430 Masala, Finland (e-mail: shaohui@ahjzu.edu.cn).

Y. Chen is with the Department of Remote Sensing and Photogrammetry, Finnish Geospatial Research Institute, FI-02430 Masala, Finland, and also with the Key Laboratory of Quantitative Remote Sensing Information Technology, Chinese Academy of Sciences (CAS), Beijing 100094, China (e-mail: yuwei.chen@nls.fi).

Z. Yang is with the Department of Computer Science, Norwegian University of Science and Technology, NO-7491 Trondheim, Norway (e-mail: zhirong.yang@ntnu.no).

C. Jiang, E. Puttnon, and J. Hyyppä are with the Department of Remote Sensing and Photogrammetry, Finnish Geospatial Research Institute, FI-02430 Masala, Finland.

W. Li and H. Wu are with the Key Laboratory of Quantitative Remote Sensing Information Technology, Chinese Academy of Sciences (CAS), Beijing 100094, China.

Z. Wen is with the State Key Laboratory of Mining Disaster Prevention and Control, Shandong University of Science and Technology, Qingdao 266590, China.

S. Wang is with the State Key Lab of Shanghai Institute of Technical Physics, Chinese Academy of Sciences (CAS), Shanghai 200083, China.

Color versions of one or more of the figures in this letter are available online at http://ieeexplore.ieee.org.

Digital Object Identifier 10.1109/LGRS.2019.2937720

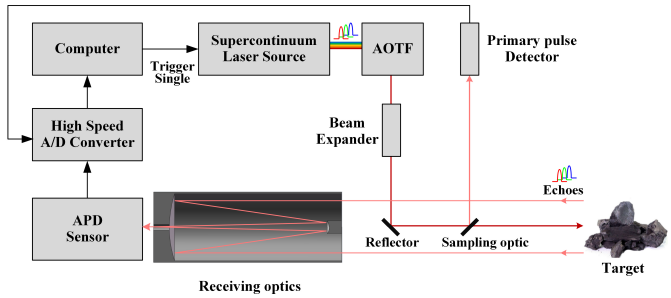

Fig. 1. Schematic illustration configuration.

classification methods: naive Bayes (NB), logistic regression (LR), and support vector machine (SVM). The four-type coal/rock specimens (coal, rock from roof layer, rock from floor layer, and gangue-rock) were collected from Wanglou coal mining, Jining, Shandong province, China, and the site depth is 1000 m underground.

Gaussian fitting (GF) technique is a commonly used methodology to improve the range performance of LiDAR waveform, especially, when the signal-to-noise (S/N) ratio is poor [12], [13]. In this letter, we try to evaluate whether/how the GF can enhance the classification results based on the spectra collected by the HSL. We conducted case studies to explore the influence of GF on AOTF-HSL.

The major contributions of this letter are listed as follows.

1) This letter reveals a 91-channel AOTF-HSL with a 5-nm spectral resolution covering from 650 to 1100 nm.
2) This letter first explores the coal/rock classification based on the AOTF-HSL spectral.
3) This letter explores the improvement of classification based on the GF method and discusses the calibration influence on coal/rock classification with reference whiteboard (RB).

The rest of this letter is organized as following four sections. Apart from the first Introduction section, an overview of the AOTF-HSL instrument and measurements are given in Section II; Section III includes the GF method and the multi-label classifiers; Section IV describes the data processing, the detailed experimental results, and the analysis of the results; and Section V concludes this letter and discusses future development.

II. Instrument and Measurements

A. AOTF-HSL

The system configuration of the 5-nm spectral resolution AOTF-HSL is designed based on the previous 10-nm spectral resolution version using a supercontinuum laser source (YSL SC-OEM) [14], as shown in Fig. 1. An AOTF model (YSL) [15] is employed in the lab test as the spectroscopic device that is installed in front of the supercontinuum laser source to select the wavelength of the emitted laser pulse at each time slot, which covers the spectrum from visible (VIS) to near-infrared (NIR). Thus, it offers both range measurement and consecutive spectral measurement from 650 to 1100 nm. A Cassegrain telescope collects the scattered laser pulse from the target and focuses it on a silicon avalanche photodiode (APD) installed on the focal point of the telescope. The output signals of the high-voltage-bias APD are recorded by a high-speed oscilloscope. The transmitted pulse is sampled by a reflector placed at the optical axis of the Cassegrain telescope, as shown in Fig. 1. The telescope also collects the scattered laser echoes from the target. By such optical design, only one APD sensor is required for the system, and the investment for hardware can be saved since less high-speed A/D converters are used.

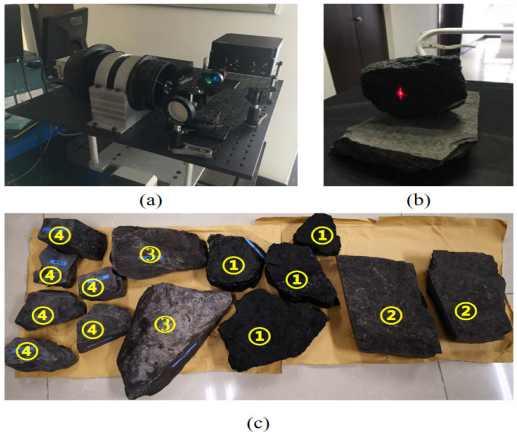

Fig. 2. Experimental setup and coal/rock specimens. (a) HSL experimental setup. (b) Coal specimen on testing. (c) Specimens (①: coal, ②: rock from roof layer, ③: rock from floor layer, and ④: gangue-rock).

B. Range Measurements

With the current experimental setting, the coal/rock specimens were put on a base with a range of 17.85 m toward the HSL, and the range was assured with a commercial Leica laser telemeter (Leica D8) by measuring the range between the Cassegrain telescope and the coal/rock targets as reference value rather than authentic value for range performance evaluation. Due to the nature of the complex optics design of the HSL, the authentic range cannot be directly derived.

C. Hyperspectral Measurements

The measurements were conducted under a controlled laboratory environment to obtain hyperspectral information and distance by AOTF-HSL, as shown in Fig. 2(a) and (b). Fig. 2(c) shows the coal/rock specimens.

In this letter, the measurements of the spectral channels were selected in a range from 650 to 1100 nm, for the low sensitivity of the APD and the low transmitted power intensity of the supercontinuum laser below 650 nm [10], [14]. The waveforms of pulses reflected from coal/rock specimens were collected by an oscilloscope operating at a 20-GHz sampling rate.

The echo intensities are normalized by applying spectral calibration with a standard whiteboard (70% reflectance, Spectralon) at the same distance as the coal/rock specimens during the lab test [16], [17], which is calculated as follows:

$$r_i(\lambda) = r_{\text{coal}_i}(\lambda) / r_{\text{panal}}(\lambda) \tag{1}$$

where r_{coal} and r_{panel} represent the specimen radiance and standard radiance at a wavelength λ.

All coal/rock specimens were in the same distance from the experimental table in test, and the laser beams were projected perpendicularly on the surface of specimens, as shown in Fig. 2(c), so the affection of the range differences of coal/rock specimens on spectra is neglectable [16].

III. Data Analysis Method

A. Gaussian Fitting

Using the Gaussian function to fit the observed data, which is commonly used in various signal processing disciplines. Due to the symmetry of a Gaussian function, the Gaussian peak position is determined very efficiently [18]. Therefore, the GF method is applied widely to calibrate the reflected pulse in LiDAR for more accurate distance measurement between the HSL and target [11]–[13].

In this letter, we fit the trigger and echo signal waveforms by using the Gaussian function [19]. Once the transmitted and return echo positions and widths are determined from the fitting waveform, distances are measured first, and then, the hyperspectral intensities are extracted by the fitted Gaussian peak heights. Furthermore, classification features are derived from the unfiltered/filtered echo waveform.

B. Classification Methods

The goal of the classification method is to understand how to map a set of input features to its corresponding output. The data provided to classification must be labeled for training. Each label represents the correct prediction for its related input. Classification methods depend on the assignments of class labels that based on their input samples and can be categorized into binary-label classifications and multi-label classifications. The multi-label classifications are increasingly required by complex task applications for their more accurate predictions.

To explore coal/rock classification based on AOTF-HSL spectra, three classifiers are used in this letter including NB [20], LR [21], and SVM [22]. The multi-label classifications are implemented by the scikit-learn Python package [23].

IV. Result and Analysis

Based on the schematic setup of the AOTF-HSL described in Section II, the range and hyperspectral measurements are conducted in the lab experiments.

A. Data Processing

The AOTF-HSL collects the original waveforms, from which the general range precision, time-of-flight (ToF) measurements, and reflectance of different spectral channels are calculated. Fig. 3 illustrates the outputted waveforms by averaging eight HSL waveforms for each spectral channel of a dedicated specimen. The waveform includes both the transmitting pulses and the echoes due to the optical design presenting in Fig. 1. To illustrate clearly, we select waveforms of ten spectral bands from 650 to 1100 nm with a 50-nm interval rather than all 91 spectral channels, as shown in Fig. 3.

From Fig. 3, we can observe that the responses after 1000 nm are weak due to the fact that the spectral sensitivity

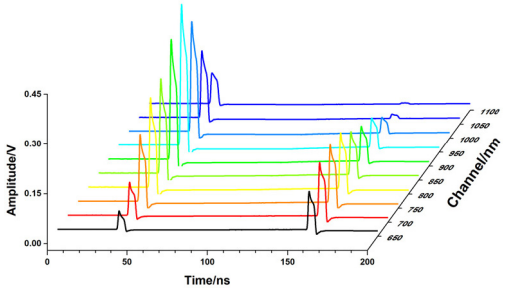

Fig. 3. Original waveforms for coal specimen (ten channels only).

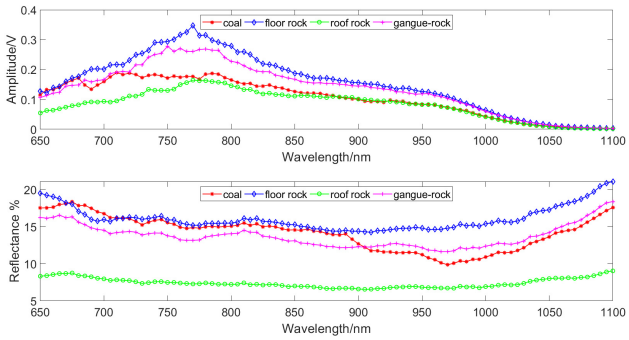

Fig. 4. Echo maximum and reflectance measurement for coal/rock specimens.

at that spectrum range of the employed silicon APD is at least one magnitude lower than its peak value (∼2.5 A/W at 1050 nm versus 50 A/W at 800 nm).

The amplitude peaks are extracted from echo waveforms as spectral measurements. We can observe from Fig. 4(a) that the difference of the maximum spectral measurements of four coal/rock specimens is slight, especially when the wavelength is beyond 1050 nm. The measurements extracted from coal and roof layer rock almost coincide with each other especially when the wavelength exceeds 875 nm, and the difference between gangue-rock and floor layer rock is minor after 950 nm, which may hinder the classification performance. As a result, classification based on an echo signal may require a more robust algorithm.

Supported by the reference board, we obtain the maximum values of reflectance after processing by employing (1), and then, the reflectance of each channel is averaged by eight measurements. Clear differences in the reflectance of spectral domain can be observed in Fig. 4(b). However, it is difficult to install the reference white panel in-site coal mining in practical operation, which is vulnerable to be contaminated with dust. It is obvious that roof layer rock specimen has considerably lower spectral reflectance values than other coal/rock specimens. Coal and floor layer rock have similar spectral profiles, especially between 700 and 900 nm. In general, the difference by utilizing the calibration board can be easily observed, which might facilitate the classification.

B. Range Performance

Range measurement is critical and determines the accuracy of the collected spatial information. As aforementioned, the referenced range is not available due to the current

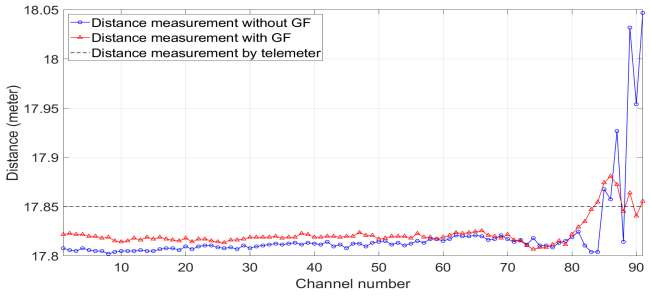

Fig. 5. Range measurements of the AOTF-HSL (coal specimen).

AOTF-HSL optical design. To determine the flying time of each pulse, the positions of the maximum amplitude of the transmitting pulse and the echo waveform are determined from the collected waveform. By multiplying the speed of light, the distance between the LiDAR and the target can be calculated.

Fig. 5 shows that the distances extracted from the waveforms of different spectral channels, and their values differ from 17.78 to 18.08 m, which are obtained by averaging of eight measurements for each spectral channel to archive better precision. The uniformity of the range measurements over all spectral channels of AOTF-HSL is evaluated and verified, but the measured distances become large after 1070 nm due to the low S/N ratio signals collected in that spectrum range. We also utilize the GF technique to process the raw waveforms, and the averaged filtered waveforms present a smoother range measurement over the spectrum as the red line with a triangle mark illustrated in Fig. 5, especially in the low S/N ratio spectral range. The average standard deviation of the distance measurements for all spectral channels is 3.89 cm without GF, and it is mitigated to 1.35 cm based on the GF technique, reducing by 65.94%. Furthermore, we divide the spectral range into two parts (Part 1: 650–1045 nm and Part 2: 1050–1100 nm). The standard deviation of the distance measurements for Part 1 is 0.48 cm without GF and further 0.38 cm with GF, reducing by 20.83%. Especially for Part 2, the standard deviation drops 83.41% from 8.86 to 1.47 cm. It is clear that the GF technique can enhance the range measurement accuracy obviously when S/N ratio is low. And even, GF can also improve the accuracy of range measurements of HSL in the high S/N ratio cases.

C. Classification Performance

In order to honestly evaluate the improvement in classification introduced by GF and reference data from RB, four test cases evaluated during the experiments using different classification features, they are as follows:

1) *CASE I*: disable GF and without RB;
2) *CASE II*: enable GF and without RB;
3) *CASE III*: disable GF and with RB;
4) *CASE IV*: enable GF and with RB.

As we suppose that both GF and the reference from RB have a positive influence on the final classification result, the classification performance should improve from CASE I to CASE IV.

TABLE I
COMPARISON OF CLASSIFICATION RESULTS BASED ON THE FOUR CASES

	NB	SVM	LR
CASE I	47	12	6
CASE II	30	7	6
CASE III	25	4	3
CASE IV	15	3	2

TABLE II
COMPARISON OF CLASSIFICATION RESULTS BASED ON THE SAME DATA SET

	NB	SVM	LR
CASE I	33.24	62.11	83.28
CASE II	33.28	71.73	91.7
CASE III	36.60	72.4	91.72
CASE IV	54.11	83.36	100

For the analysis of classification results, we used 50% samples (11 000) for training data set and the remaining 50% samples (11 000) for testing data set, and the labels were set as {0, 1, 2}.

Table I presents the comparison of results by three classifiers with different feature cases. The number in Table I indicates the minimum number of spectral channels (MNSCs) used to acquire 100% classification accuracy. According to the classification experimental results, all classifiers can achieve 100% classification accuracy when the training data are sufficient.

It is worth noticing that the GF method effectively improves the classification result, especially for NB and SVM classifies. Based on the NB classifier, the MNSC needed to reach 100% accuracy with CASE II decrease from 47 channels for CASE I to 30, reducing by 36.17%. Furthermore, supported by the RB, the required MNSC considerably decreases to 25 without GF and further 15 with GF, respectively. The similar promising results based on the SVM classifier can also be found that the MNSC drops from 12 to 7, 4, and 3, which indicates that the classification can be fulfilled by a reference-board-enabled dual-wavelength LiDAR. It is a meaningful finding that GF can improve the classification result from HSL measurements, for the GF method may eliminate noise and clutter signal to enlarge the difference of classification feature.

Table II lists the classification accuracy (%) of three classifiers with different cases based on the same data set (two channels). It can be seen that a higher accuracy with GF exceeds echo maximum value only, and the increments vary with classifiers, such as 0.04% in NB, 9.12% in SVM, and 8.42% in LR; Compared to CASE I, the results based on RB improve 3.36%, 10.29%, and 8.44%, respectively. The results based on CASE IV outperform other cases. Compared to CASE I, the classification results of the three classifiers

increase by 20.87%, 21.25%, 16.72%, respectively. We can draw a conclusion that RB is beneficial for classification; also, combing with GF can further improve the classification results. When there are no calibration data available, GF technique might improve the classification performance.

As can be observed, the classification performance of NB classifier is worst among these classifiers. The explanation is straightforward: the attribute independence assumption harms NB classification performance when it is violated in reality as we have known [20]. SVM can reach desirable classification accuracy for HSL derived spectra. Also, it is worth noticing that the multiple LR classifier stands out by having the fewest channels reach 100% accuracy, which outperforms the other two selected classifiers.

V. Conclusion

In this letter, HSL covering spectrum range from 650- to 1100-nm-based AOTF is presented, offering consecutive spectral measurements with a 5-nm spectral resolution and range measurement with 7.5-mm range resolution. Then, we present a feasibility study using the AOTF-HSL for coal/rock specimens classification, which were collected in the underground coal mining environment. Classification with three standard multi-label classifiers NB, SVM, and LR is investigated. The case study is conducted to explore the influence of availability of the calibration data and the GF technique. Finally, we draw the following conclusion.

1) GF can not only improve the accuracy of range measurement but also enhance the classification result no matter whether the calibration data are available or not, the noise mitigation functionality offered by the GF technique might improve the classification performance. It has not been reported before in HSL to the authors' best knowledge.
2) The performance drop in the calibration-free classification can be compensated to some extent by utilizing the GF technique. However, a more robust classification method under calibration-free condition is worthy of further investigation.
3) The selection of suitable classifier is also critical for HSL-based classification due to the nature of data.
4) Calibration with whiteboard is effective to improve the classification accuracy, but it may be difficult to obtain under a practical operation condition.

Although only four types of coal/rock specimens are investigated in this letter, the results can be considered suggestive. More rocks and other types of material utilized in coal mining environment will be further investigated for sounder research.

References

[1] Q. Feng and H. Chen, "The safety-level gap between China and the US in view of the interaction between coal production and safety management," *Saf. Sci.*, vol. 54, pp. 80–86, Apr. 2013.

[2] R. Kukutsch, V. Kajzar, P. Konicek, P. Waclawik, and J. Ptacek, "Possibility of convergence measurement of gates in coal mining using terrestrial 3D laser scanner," *J. Sustain. Mining*, vol. 14, no. 1, pp. 30–37, 2015.

[3] C. Bingqian, D. Kazhong, F. Hongdong, and H. Ming, "Large-scale deformation monitoring in mining area by D-InSAR and 3D laser scanning technology integration," *Int. J. Mining Sci. Technol.*, vol. 23, no. 4, pp. 555–561, Jul. 2013.

[4] R. Kukutsch, V. Kajzar, P. Waclawik, and J. Nemcik, "Use of 3D laser scanner technology to monitor coal pillar deformation," in *Proc. 16th Coal Operators Conf. Mining Eng.*, Wollongong, NSW, Australia, Feb. 2016, pp. 98–107.

[5] I. Trinks *et al.*, "Digital rock art recording: Visualising petroglyphs using 3D laser scanner data," *J. Rock Art Res.*, vol. 22, no. 2, pp. 131–139, 2005.

[6] V. Kajzar, R. Kukutsch, and N. Heroldova, "Verifying the possibilities of using a 3D laser scanner in the mining underground," *Acta Geodynamica et Geromaterialia*, vol. 12, no. 1, pp. 51–58, Feb. 2015.

[7] J. Hyyppa, L. Matikainen, H. Kaartinen, X. Yu, H. Hyyppa, and P. Ronnholm, "Improving automation in map updating based on national laser scanning, classification trees, object-based change detection and 3D object reconstruction," in *Proc. Urban Remote Sens. Joint Event*, Paris, France, Apr. 2007, pp. 1–10.

[8] C. Reymann and S. Lacroix, "Improving LiDAR point cloud classification using intensities and multiple echoes," in *Proc. IEEE/RSJ IROS*, Hamburg, Germany, Sep./Oct. 2015, pp. 5122–5128.

[9] C. Yuwei *et al.*, "Two-channel hyperspectral LiDAR with a supercontinuum laser source," *Sensors*, vol. 10, no. 7, pp. 7057–7066, Jul. 2010.

[10] Y. Chen *et al.*, "Feasibility study of ore classification using active hyperspectral LiDAR," *IEEE Geosci. Remote Sens. Lett.*, vol. 15, no. 11, pp. 1785–1789, Nov. 2018.

[11] T. Hakala, J. Suomalainen, S. Kaasalainen, and Y. Chen, "Full waveform hyperspectral LiDAR for terrestrial laser scanning," *Opt. Express*, vol. 20, no. 7, pp. 7119–7127, Mar. 2012.

[12] E. Puttonen *et al.*, "Artificial target detection with a hyperspectral lidar over 26-h measurement," *Opt. Eng.*, vol. 54, no. 1, 2015, Art. no. 013105.

[13] J. Vauhkonen *et al.*, "Classification of spruce and pine trees using active hyperspectral LiDAR," *IEEE Geosci. Remote Sens. Lett.*, vol. 510, no. 5, pp. 1138–1141, Jan. 2013.

[14] Y. Chen *et al.*, "A 10-nm spectral resolution hyperspectral LiDAR system based on an acousto-optic tunable filter," *Sensors*, vol. 19, no. 7, p. 1620, Apr. 2019.

[15] *Datasheet of YLS AOTF*. Accessed: Mar. 2017. [Online]. Available: http://www.yslphotonics.com/Uploads/UserFile/File/19/20170331/58de7c3d8c7c1.pdf

[16] E. Puttonen *et al.*, "Tree species classification from fused active hyperspectral reflectance and LIDAR measurements," *Forest Ecol. Manage.*, vol. 260, no. 10, pp. 1843–1852, 2010.

[17] L. Du, W. Gong, and J. Yang, "Application of spectral indices and reflectance spectrum on leaf nitrogen content analysis derived from hyperspectral LiDAR data," *Opt. Laser Technol.*, vol. 107, pp. 372–379, Nov. 2018.

[18] H. Guo, "A simple algorithm for fitting a Gaussian function [DSP tips and tricks]," *IEEE Signal Process. Mag.*, vol. 28, no. 5, pp. 134–137, Sep. 2011.

[19] W. Wagner, A. Ullrich, V. Ducic, T. Melzer, and N. Studnicka, "Gaussian decomposition and calibration of a novel small-footprint full-waveform digitising airborne laser scanner," *ISPRS J. Photogramm. Remote Sens.*, vol. 60, no. 2, pp. 100–112, Apr. 2006.

[20] K. M. Al-Aidaroos, A. A. Bakar, and Z. Othman, "Naïve bayes variants in classification learning," in *Proc. CAMP*, Selangor, Malaysia, Mar. 2010, pp. 276–281.

[21] S. Dreiseitl and L. Ohno-Machado, "Logistic regression and artificial neural network classification models: A methodology review," *J. Biomed. Inform.*, vol. 35, nos. 5–6, pp. 352–359, 2002.

[22] C. Baumgartner *et al.*, "Supervised machine learning techniques for the classification of metabolic disorders in newborns," *Bioinformatics*, vol. 20, no. 17, pp. 2985–2996, Nov. 2004.

[23] F. Pedregosa *et al.*, "Scikit-learn: Machine learning in Python," *J. Mach. Learn. Res.*, vol. 12, pp. 2825–2830, Oct. 2011.